Materials & Design 213 (2022) 110336

Contents lists available at ScienceDirect

Materials & Design

journal homepage: www.elsevier.com/locate/matdes

Thermomechanical simulation of the heat-affected zones in welded ultra-high strength steels: Microstructure and mechanical properties

Shahriar Afkhami [a], Vahid Javaheri [b], Mohsen Amraei [c,f,*], Tuomas Skriko [d], Heidi Piili [c,f], Xiao-Ling Zhao [e], Timo Björk [a]

[a] Laboratory of Steel Structures, LUT University, P.O. Box 20, 52850 Lappeenranta, Finland
[b] Materials and Mechanical Engineering, University of Oulu, 90014, Finland
[c] Laboratory of Laser Materials Processing and Additive Manufacturing, LUT University, Lappeenranta 53850, Finland
[d] Laboratory of Welding Technology, LUT University, P.O. Box 20, 53851 Lappeenranta, Finland
[e] The School of Civil and Environmental Engineering, UNSW Sydney, NSW 2052, Australia
[f] Department of Mechanical and Materials Engineering, University of Turku, Turku, 20520, Finland

HIGHLIGHTS

- Thermomechanical simulation using Gleeble proved to be a reliable approach to replicate and reconstruct HAZ subzones.
- Ferrite and granular bainite as the primary cause behind the HAZ softening.
- Acceptable reliability of the hardness models based on microstructures to predict soft zones.
- Controversial simultaneous decrease in hardness and toughness was associated with carbide precipitation in tempered phases.

GRAPHICAL ABSTRACT

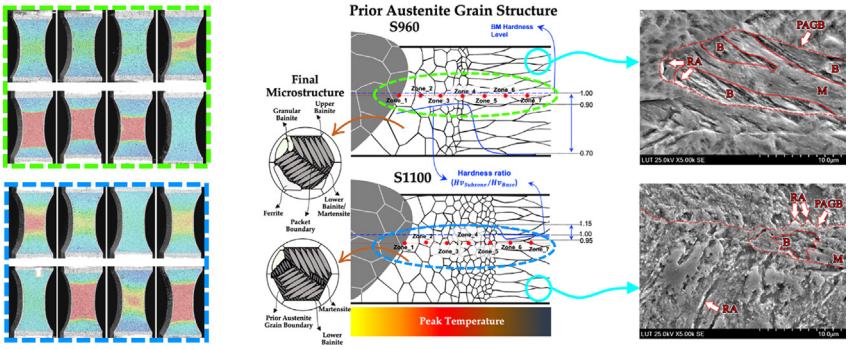

ARTICLE INFO

Article history:
Received 20 September 2021
Revised 13 December 2021
Accepted 19 December 2021
Available online 21 December 2021

Keywords:
Ultra-high strength steel
Heat-affected zone
Mechanical properties
Microstructure

ABSTRACT

Ultra-high strength steels (UHSS) have a determining role in construction and industry. Furthermore, welding as the primary joining process for steel has a similar role in promoting its applications. Therefore, welded UHSS have a vital role in related applications. However, due to their complex microstructures, these steels are more prone to harmful effects of welding heat input on the mechanical properties compared to mild steels. Thus, identifying the correlations between the microstructural transformations triggered by the heat input and the mechanical properties can lead to new insights and hindering the drawbacks. This study investigates the microstructures and mechanical properties of S960 (with a severe softening after welding) and S1100 (with a negligible decrease of the mechanical properties after welding) to understand the mechanisms behind the softening of welded UHSS. Microstructural analysis showed the formation of soft phases, e.g., ferrite and granular bainite, as the primary reason for the softening. Furthermore, tempered forms of martensite and bainite resulted in the simultaneous decrease of hardness and notch toughness. Finally, the applicabilities of two experimental approaches to predict hardness from microstructural constituents were evaluated for welded S960 and S1100 and proved to have relatively good reliability to detect their HAZ softened spots.

* Corresponding author.
E-mail address: Mohsen.Amraei@lut.fi (M. Amraei).

https://doi.org/10.1016/j.matdes.2021.110336
0264-1275/

1. Introduction

Steel, as a pivotal engineering material, is vital to metal structures. Various sectors such as transportation, shipbuilding, and the construction are heavily dependent upon this material. These resource-intensive industries are currently more focused on effectively protecting the environment and sustainable development due to the contemporary natural crisis associated with climate change and high carbon emissions. In order to achieve these goals, natural resources should be used more efficiently, energy consumption and carbon emission should be reduced, and material waste has to be minimized. Thus, modern steel structures and components should be more energy-efficient and withstand higher extreme natural loads to extend service life [1,2]. This necessity accentuates the importance of the new generation of micro-alloyed steels with ultra-high strength levels and simple chemical compositions, along with efficient and economical manufacturing processes of these steels, since they make it possible to build cost-efficient and robust steel structures with significant strength-to-weight ratios [3].

According to the current definition, steels with minimum nominal yield strength higher than 700 MPa are known as ultra-high strength steels (UHSS). As a type of advanced high strength steels (AHSS), these metals consist of complex multiphase microstructures that obtain good combinations of strength and ductility by grain refinement through thermomechanical processing techniques, e.g., a reiterative combination of rolling, tempering, or quenching cycles. The resultant microstructure usually is a combination of ferrite, bainite, martensite, and retained austenite [4–6]. These steels have become popular in typical industrial applications; However, the available range of their strength is not fixed yet due to their constant development. The current yield limit of UHSS has reached above 1400 MPa, and it improves progressively. Therefore, their domain of applications becomes wider every day [3,6].

To leverage the most from UHSS in demanding applications, welding as a common joining technique for steel structures and components is vital. However, due to the thermomechanical strengthening mechanisms and complex nature of the microstructures of these steels, UHSS are more prone to the adverse effects of welding on their properties compared to conventional carbon steels with lower strength ranges [2,3,7]. Welding heat input (HI) exposes UHSS to microstructural transformations that are not in favor of the mechanical performance of their welded joints. These transformations affect the hardness, ductility, or strength of the materials in their heat-affected zone (HAZ) [8–10]. Therefore, characterizing the microstructures and identifying their influential evolutions before and after welding are essential to recognize the adverse effects of this process and hinder them while joining UHSS [11].

Numerous studies have been recently focused on welding of UHSS and the effects of HI on their microstructures and properties [2,3,11–15]. According to these investigations, a decrease in strength and hardness in the HAZ, generally known as HAZ softening, is the most severe drawback associated with welded UHSS, causing up to 60% loss in the hardness or strength [11,16]. This negative effect is especially highlighted in low alloy direct-quenched types of UHSS. This degradation of the mechanical properties is due to the microstructural changes that result in undesirable phases in the HAZ, which are triggered by the welding HI. Furthermore, some other properties of welded joints in UHSS, e.g., toughness and load-bearing capacity, are also proved to rely on HI and its resultant microstructure [2,7,11,17–19]. However, it is possible to minimize the harmful effects of HI by controlling it to prevent or limit unwanted microstructural transformations. Therefore, the undesirable transformations and their resultant microstructures should be recognized in the first place to assist this approach [3,11].

According to the literature, HAZ in welded UHSS can be divided into several subzones depending on their microstructures and distances from the fusion line. The distance determines the peak temperature (T_{peak}) and cooling rate each subzone goes through to reach its final microstructure and mechanical properties. These subzones usually include coarse-grain (CG), fine-grain (FG), inter-critical (IC), and sub-critical (SC) HAZs. Each subzone could have its unique physical and mechanical characteristics differing from those of others and might act as a weak point through the welded area. Hence, it is crucial to evaluate each subzone independently to thoroughly analyze the behavior of HAZ as a whole [2,3,11,20].

Most of the investigations in the literature are focused on the overall performance of welded joints. Therefore, in a preceding study, the mechanical properties of each individual HAZ subzone following the unique thermal cycle it experienced through a gas metal arc welding (GMAW) procedure, as a commonly used industrial welding process, were investigated [11]. However, the microstructural transformations and their mechanisms were excluded since they were out of the scope of that research. Hence, the current study examines the microstructure of each subzone individually to evaluate the HAZ. In the present study, the microstructural transformations, their resultant microstructures, and their correlation to the mechanical properties are probed via independent thermomechanically reconstructed samples. Consequently, the link between the welding HI and the microstructures is assessed to understand the harmful effects of welding on UHSS. For this purpose, two types of UHSS, S960 (with a relatively high softening at its HAZ) and S1100 (with a relatively negligible HAZ softening), are chosen to provide the reader with a reasonable comparison to understand which microstructural transformations resulted in the mechanical deterioration. These two UHSS grades have different alloying and manufacturing processes. While the S960 is manufactured via direct quenching, the S1100 has gone through a quenched and tempering process.

2. Materials and methods

In this study, the HAZs of S960 and S1100 structural steels are divided into seven distinct subzones for close examination based on their distance from the weld fusion line. The peak temperature and cooling rate associated with each subzone are presented in Table 1. A Gleeble 3800 thermomechanical simulator was used to simulate these subzones. Further information on the time–temperature data of the reconstructed regions is presented in [11]. The as-received materials were cut into 55 mm × 10 mm × 5 mm blocks to fit in the simulator copper grips. The free span was of about 22 mm and the thermocouple was placed exactly in the mid-length of specimen. The thermal cycles of each subzone were simulated based on the welding parameters presented in Table 2. These welding parameters represent an actual GMAW process typically used in industrial applications. The hardness values of the

Table 1
Time-temperature data of the simulated HAZ subzones [11].

Subzone number	Estimated distance from the fusion line (mm)	Approximated peak temperature (°C)	$\Delta t_{8/5}$ (s)
1	0.0	1350	10.3
2	0.5	1154	10.4
3	1.0	1000	10.5
4	1.5	890	10.7
5	2.0	800	11.6
6	2.5	730	–
7	3.0	670	–

Table 2
Welding variables determining the Gleeble thermal cycles [11].

Variable	Welding potential(V)	Welding current(A)	Welding speed(mm/s)	Linear heat input(kJ/mm)
Value	25	220	6.2	0.7

samples were measured with a Struers DuraScan 70 by applying 5 kgf for 15 s. After that, the middle sections of the samples were ground sequentially with different abrasive pads (up to 2000 grit) and polished using 1 μm colloidal silica. Nital etchant with 15 s soaking time was used to reveal the microstructural features of the samples by scanning electron microscopy (SEM). SEM was performed with a SU3500 microscope from Hi-Tech Instruments. Continuous cooling transformation (CCT) diagrams of the materials were modeled by the JMatPro software package using the chemical compositions of S960 and S1100 provided as certificates by their manufacturer (Table 3).

A field emission scanning electron microscope (FESEM-ZEISS, SIGMA) was employed for the electron backscatter diffraction (EBSD) measurements. In addition to the described sample preparation for SEM, an additional polishing step using 0.04 μm colloidal silica was carried out on the EBSD samples. The EBSD measurements were performed using an accelerating voltage of 15 kV, a working distance of 15 mm, and a scanning step size of 0.2 μm. The data were acquired from an area size of 220 μm × 220 μm.

Image quality (IQ) data from the EBSD results (EBSD-IQ) was used, in addition to the SEM qualitative analysis, to have a more reliable identification and quantification of the microstructural features. As reported in [21–23], different phases and microstructural constituents produce distinct IQ values in EBSD measurements. The distinction is because of the varying dislocation networks and densities of each microstructural feature. Hence, quantitative analysis of microstructures can be performed by analyzing the numerical values of EBSD-IQ. For this purpose, based on the previous work by DeArdo [24,25], IQ histograms were normalized and then deconvoluted into multiple peaks as the representatives of different phases by assuming a normal distribution. Then, each unique peak was assigned to a specific microstructure component according to its position in the normalized IQ value axis. Then, the fraction of each microstructural constituent was calculated as the ratio of the area below each peak to the total normalized IQ area.

Regarding the quasi-static tensile tests, the blocks processed with the Gleeble 3800 were mechanically machined to test specimens following the dimensions shown in Fig. 1 (a). These dimensions were selected since they are compatible with the sample size limitations associated with the Gleeble machine. The tests were carried out at room temperature (≈ 20 °C), with a 150 kN test rig, under the constant strain rate of 5×10^{-4} s^{-1}. The digital image correlation (DIC) technique was utilized using an ARAMIS system to compare local strain values in the center of the gauge areas. Finally, Charpy impact toughness tests were conducted at room temperature on specimens with dimensions shown in Fig. 1 (b). Due to the limited thickness of the base materials in their original forms (8 mm thick plates), sub-size samples were used for both tensile and Charpy tests. The Charpy specimens were per the Annex A3 of ASTM E23 [26].

3. Results

The microstructures of the base metals and their simulated HAZ subzones comprised several microstructural features, including (polygonal) ferrite, various bainitic morphologies (i.e., granular, upper, and lower bainite), lath-structured martensite, and retained austenite. After welding, the constituent fractions of these features depended upon the base metal microstructures and their prior austenite grains (as material dependant parameters) and the distance from the fusion line determining the thermal gradients [11]. Data achieved via SEM, FESEM, and EBSD are presented in Sections 3.1 and 3.2. These results were simultaneously employed to analyze and quantify microstructural features from each subzone accurately.

3.1. Microstructural features

Microstructures of S960 and S1100 in their as-received condition are presented in Figs. 2 and 3, respectively. According to Fig. 2, S960 consisted of a mixture of bainite (B), martensite (M), and small sporadic islands of retained austenite (RA) arranged along the prior austenite grain boundaries (PAGB). PAGBs are marked by red dashed lines in all the figures. According to [27], martensite in microalloyed steels with complex chemical compositions, e.g., S960 and S1100, is an ultra-fine mixture of martensite/austenite (MA) with a distinct un-etched smooth appearance in SEM images. In such a mixture, retained austenite is trapped between the small laths of martensite. However, these fine features are not visible under magnifications commonly used in SEM analysis. Thus, these microstructural features are marked as martensite (M) in the images from the current study since SEM data are used for microstructural evaluations. Similar to S960, the microstructure of S1100 comprised a mixture of bainite and martensite with small islands of retained austenite scattered along the boundaries (Fig. 3).

Microstructural features of HAZ subzones from S960 are presented in Figs. 4 and 5, following their sequence and distance from the fusion line. According to these figures, the subzones of S960 comprised different mixtures of ferrite (F), bainite, lath martensite, tempered martensite (TM), bainitic ferrite (BF), granular bainite (GB), and retained austenite. However, the fractions of these features were different in each subzone following the unique thermal cycle it endured through the simulation procedure using the Gleeble machine. Microstructural features of HAZ subzones from S1100 are presented in Figs. 6 and 7. The subzones of S1100 were different mixtures of martensite, bainite, tempered martensite, autotempered martensite (AM), and bainitic ferrite. All the microstructural features mentioned for S960 and S1100 HAZ subzones were confined between prior austenite grain boundaries.

Table 3
Chemical compositions of the base materials according to their certificates.

Material	C (wt%)	Si (wt%)	Mn (wt%)	P (wt%)	S (wt%)	V (wt%)	Cu (wt%)	Cr (wt%)	Ni (wt%)	Mo (wt%)	CEV (wt%)
S960	0.088	0.040	1.130	0.010	0.000	0.009	0.011	1.000	0.050	0.117	0.590
S1100	0.133	0.192	1.490	0.006	0.001	0.152	0.437	1.340	0.998	0.388	0.850

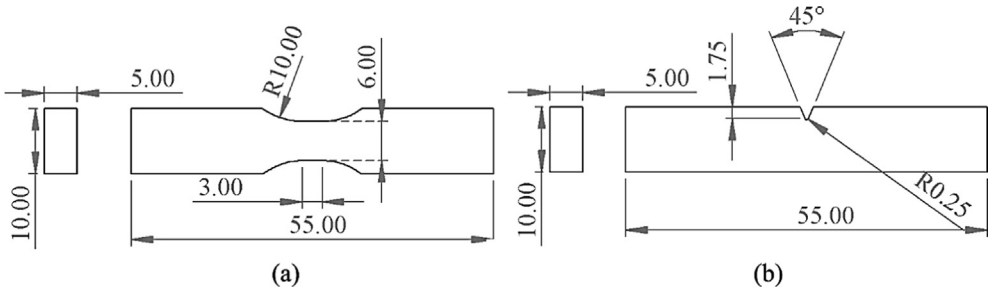

Fig. 1. Schematic views of sub-size (a) tensile and (b) Charpy specimens (lengths and angles are in mm and degree, respectively).

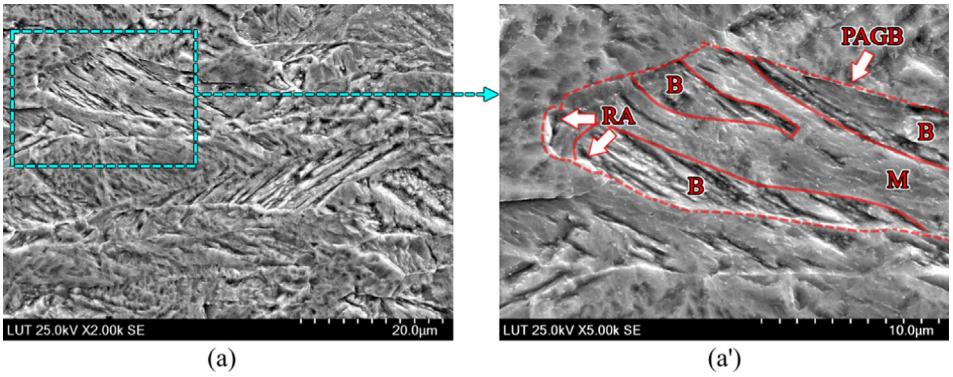

Fig. 2. Microstructure of S960 in its as-received condition: (a) 2000 × and (a') 5000×.

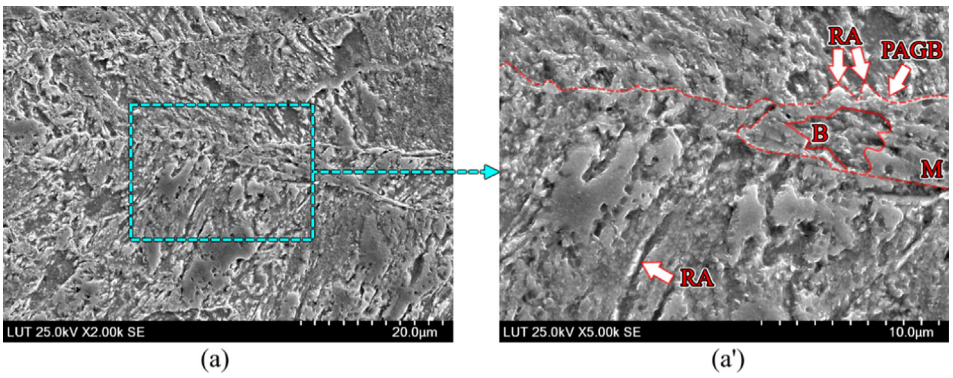

Fig. 3. Microstructure of S1100 in its as-received condition: (a) 2000 × and (a') 5000×.

3.2. EBSD results

Inverse pole figure (IPF) maps of the subzones from S960 and S1100 are presented in Fig. 8. The size of PAGBs from different subzones can be evaluated and compared accurately by the average values of equivalent circle diameters (ECD). The ECD measurements from the HAZ subzones in this study are presented in Fig. 9. According to the results, the microstructure of each subzone differed from those of the others in terms of the type and size of the microstructural features and the size of the PAGBs. The differences in these features from the subzones can be attributed to their different thermal histories. Each HAZ subzone had its unique peak temperature and cooling rate according to its distance from the fusion line (Table 1).

In order to characterize the final microstructure and quantify the fraction of each microstructural component, the EBSD-IQ data were analyzed using the method developed by DeArdo [24]. Pattern or image quality (IQ) maps obtained from the EBSD measurements can potentially reveal more structural features than secondary electron images since they represent the quality of acquired diffraction patterns [21,22]. IQ values might be affected by microstructural characteristics, surface topology, local chemistry, or residual plastic deformations [28,29]. Consequently, compared to typical SEM images, IQ analysis can provide more information about the microstructural features. In general, accumulated strains in a crystal lattice are the primary parameter that alters IQ values throughout the lattice microstructure. These strains are predominantly caused by dislocations, and there is a direct relationship between the strain values and dislocation densities. Consequently, changes in IQ values can also represent fluctuations in dislocations densities. Hence, a microstructure component with a high dislocation density results in a low IQ-valued region in its EBSD measurements and vice versa.

In steels similar to S960 and S1100, under continuous cooling regimes (similar to those that the materials experience through welding procedures), the IQ values of the transformed

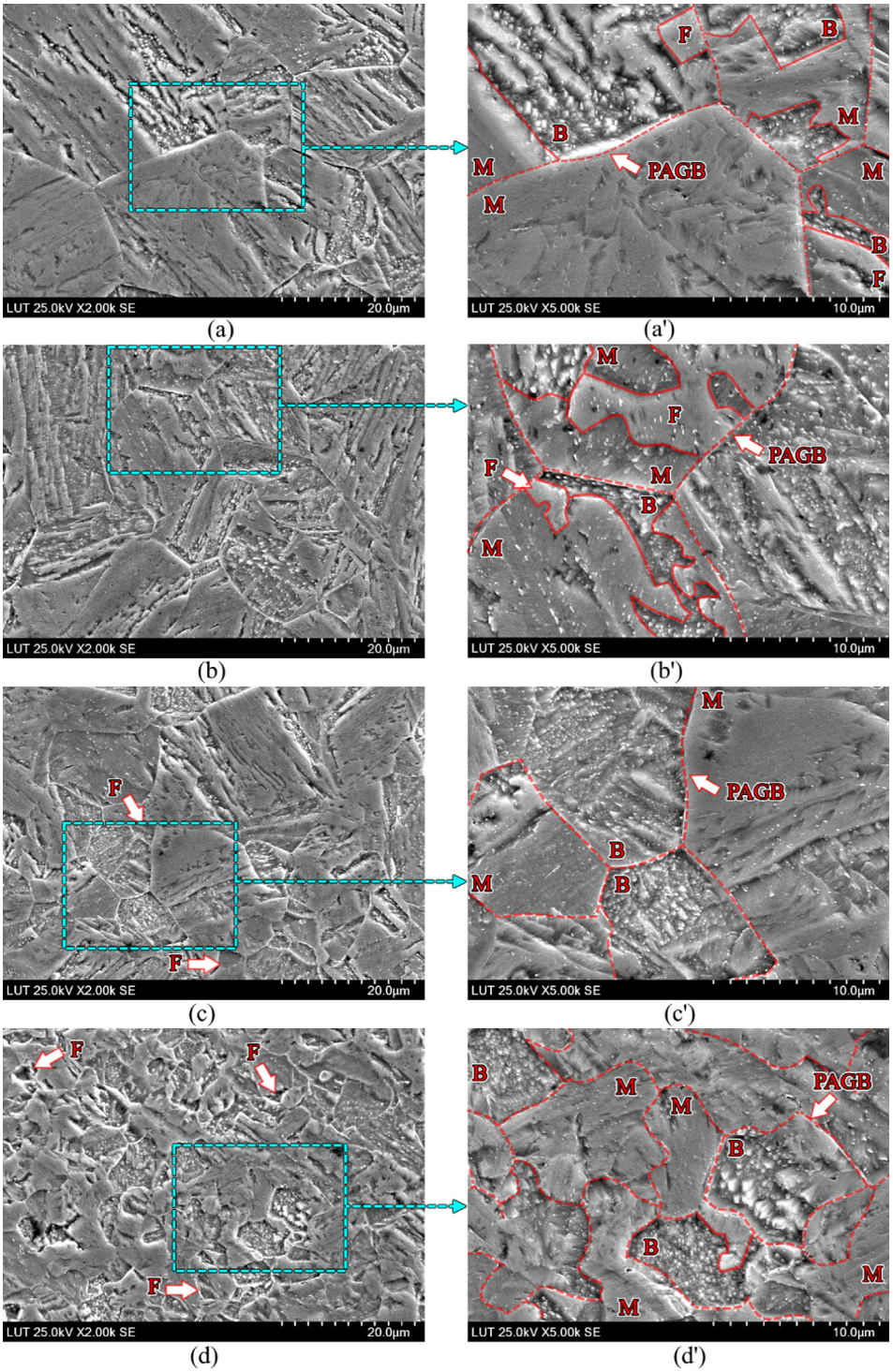

Fig 4. Microstructural features from the simulated HAZ of S960: subzones 1 (a, a'), 2 (b, b'), 3 (c, c'), and 4 (d, d').

microstructural components decrease following their transformation temperatures. The IQ values of (polygonal) ferrite are the highest, and the values drop sequentially from ferrite to granular bainite, upper bainite, lower bainite, and martensite. Thus, the IQ curves can be deconvoluted to distinct sub-curves depending on the number of potential microstructural components [24,30]. The position of each deconvoluted peak in the normalized IQ axis (from 0 to 100), which was used to identify the components, can be described as follows: 70–80 for (Polygonal) ferrite and granular bainite, 50–70 for upper bainite, 30–40 for lower bainite and martensite, and 20–30 for tempered initial microstructure. In this approach, the areal ratio of each curve under the normalized IQ curve determines the fraction of its representative phase or morphology, as shown in Fig. 10 for subzones of S960 as an example. Phase fractions achieved via this approach are presented in Fig. 11 (a) and (b) for S960 and S1100, respectively.

3.3. Local strains, hardness, and notch toughness

The local strains of HAZ subzones under fixed quasi-static loads, in addition to their hardness and notch toughness values, were measured to compare these regions regarding their mechanical

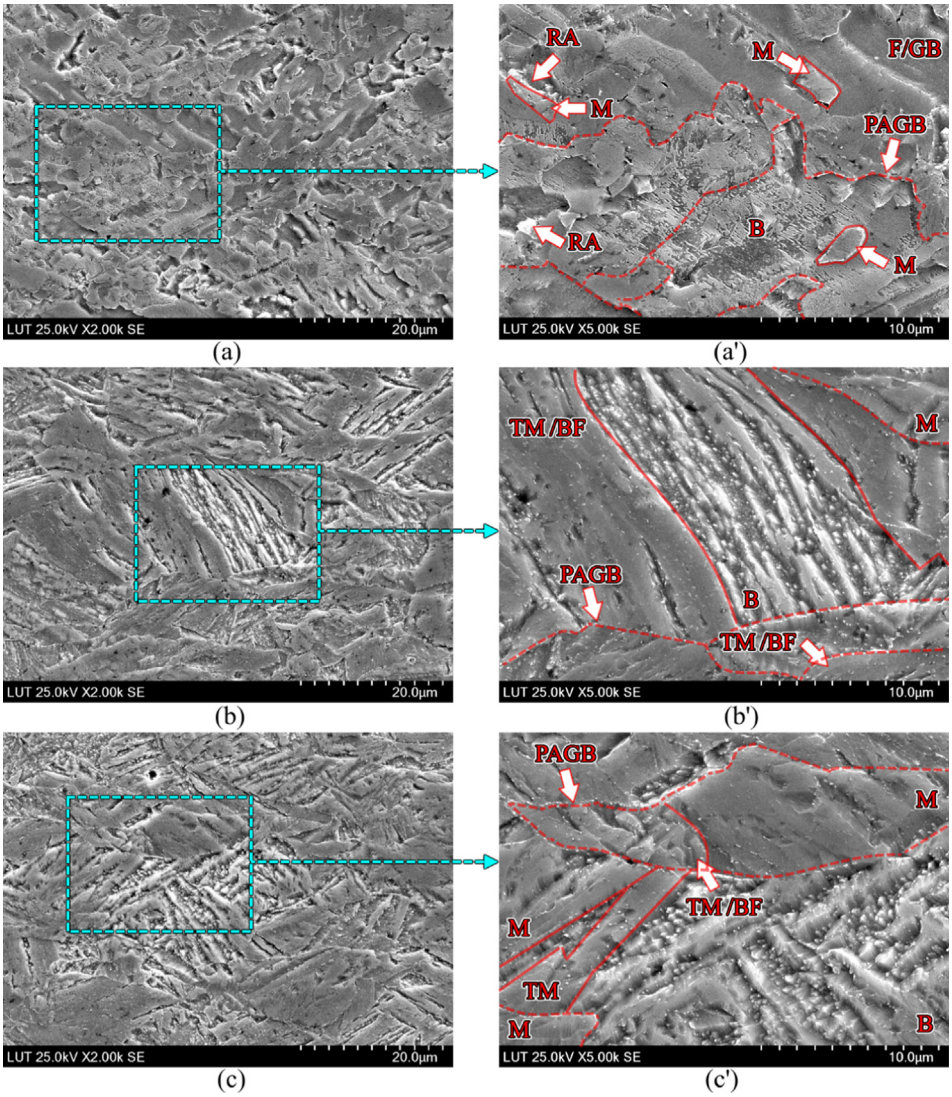

Fig. 5. Microstructural features from the simulated HAZ of S960: subzones 5 (a, a'), 6 (b, b'), and 7 (c, c').

properties. The comparison made it possible to understand a correlation between the mechanical behavior of the subzones and their microstructures, as this is discussed in Section 4.2. The local strain ranges under a fixed quasi-static load are shown for S960 and S1100 in Figs. 12 and 13, respectively. The value of the fixed load was chosen following the tensile strength of the weakest specimen (subzone) for each steel grade. The hardness and notch toughness values were extracted from the preceding study introduced in Section 1 and are presented in Fig. 14 (a) and (b), respectively [11].

4. Discussion

The expected microstructural transformations and features in the HAZs of S960 and S1100 can be identified via their CCT diagrams. The estimated CCT diagrams of S960 are presented in Fig. 15. Considering the austenitization-finish temperature (A3) of S960, HAZ subzones of this steel can be divided into two groups. The first group consisting of subzones 1 to 4, with peak temperatures higher than A3, experienced full austenitization, while the rest had partial (subzones 5–6) to no austenitization (subzone 7) depending on their peak temperatures. According to Fig. 15 (a), subzone 1 is expected to comprise a mixture of martensite, bainite, and some amount of ferrite. All these features are confined within coarse prior austenite grains resulted from the very high peak temperature of this subzone. This evaluation agrees with the SEM data shown in Fig. 4 (a) and (a').

After region 1, subzones 2, 3, and 4 had the highest peak temperatures sequentially and experienced microstructural evolutions similar to subzone 1. Consequently, they also comprised a mixture of martensite, bainite, and ferrite. However, due to their different peak temperatures, the prior austenite grain size decreased from zone 1 to 4 (Fig. 4 (a), (b), (c), and (d)). This expectation agrees with the experimental results shown in Fig. 4 (d, d') and 9 (b). The summation of these microstructural modifications (changes in prior austenite grain sizes and phase ratios) did not cause any significant changes in the hardness values, and only limited fluctuations were observed in these areas (further discussion can be found in Section 4.2) [11].

The second type of HAZ subzones consists of zones 5, 6, and 7. These areas did not reach the full austenitization temperature range. Although Subzone 5 had a peak temperature close to A3, the cooling rate was not high enough to favor martensite or lower bainite formation. Thus, austenite to ferrite, granular bainite, and upper bainite transformations were more expected. Consequently, this area was a combination of ferrite/granular bainite, fragments

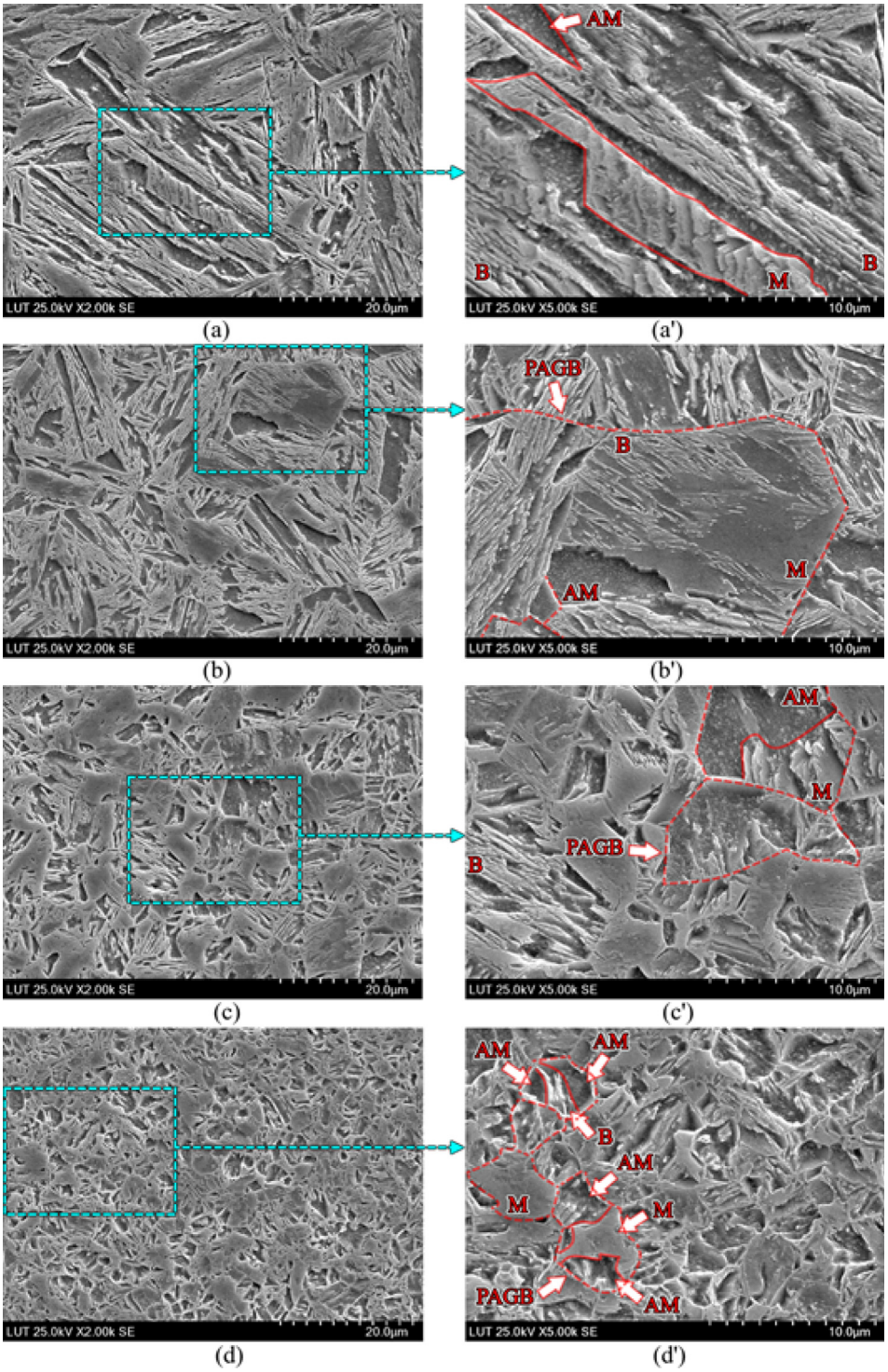

Fig. 6. Microstructural features from the simulated HAZ of S1100: subzones 1 (a, a'), 2 (b, b'), 3 (c, c'), and 4 (d, d').

of tempered martensite or bainitic ferrite, a small amount of fine-textured fresh bainite (as a result of partial austenitization and low cooling rate), and a small number of retained austenite islands sporadically scattered throughout the microstructure (Fig. 5 (a, a')). The ferrite/granular bainite formation and decline in martensite/lower bainite contents in this area resulted in a sudden drop in its hardness and the existence of a soft spot in the HAZ (generally known as softened zone).

Regarding subzone 6, the maximum temperature barely passed A1. Thus, a minor austenitization is expected to occur in this area. Furthermore, the limited cooling rate of the area is more in favor of bainite formation than martensite. Consequently, the microstructure consists of tempered martensite and bainitic ferrite originating from the base metal and fragments of fresh bainite resulting from the limited partial austenitization (Fig. 5 (b, b')). Although the hardness drop from zone 5 recovered a little due to the absence

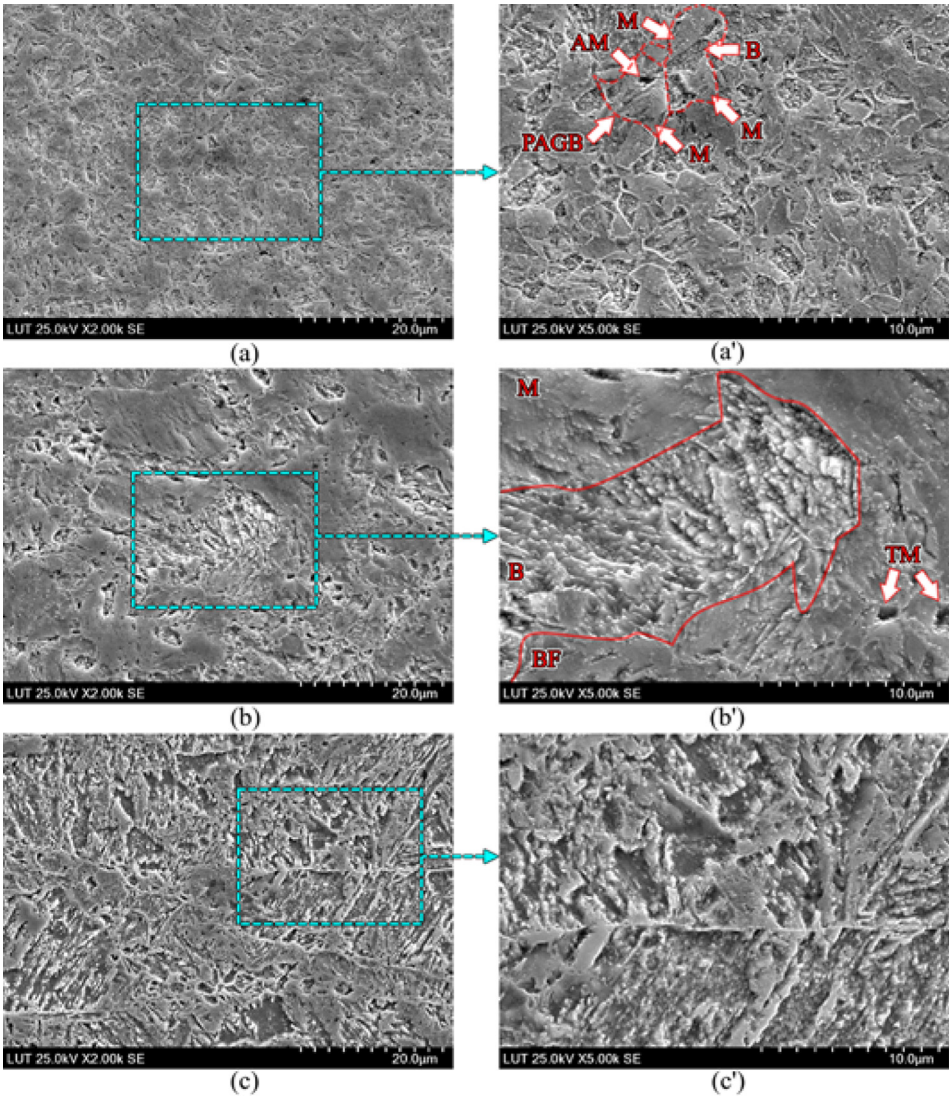

Fig. 7. Microstructural features from the simulated HAZ of S1100: subzones 5 (a, a'), 6 (b, b'), and 7 (c, c').

of ferrite in region 6, tempered microstructure did not cause a significant increase in the hardness since tempered martensite and bainite are known to be relatively soft mixtures compared to their original states.

Finally, subzone 7, as the boundary between HAZ and the base metal, experienced peak temperatures as high as 670 °C and did not pass any critical temperature through its heating cycle. Thus, the microstructural features of subzone 7 consisted of tempered martensite and bainitic ferrite, in addition to some amount of martensite and bainite remaining from the initial microstructure (Fig. 5. (c, c')). This mixture resulted in hardness values similar to that of subzone 6. In addition, white precipitates arranged along the high angle boundaries in subzones 6 and 7, especially 7 in Fig. 5 (c'), are due to the tempered microstructural features in these areas.

The CCT diagrams of S1100 are presented in Fig. 16. Similar to S960, HAZ subzones of S1100 can be divided into two groups of fully austenitized (subzones 1, 2, 3, 4, 5) and not fully austenitized (6 and 7) areas, depending on their heating cycles and peak temperatures. According to Fig. 16, there is no austenite to ferrite transformation through the cooling stage of S1100, unlike S960. Thus, the microstructures of these subzones mainly comprised mixtures of bainite and martensite. In addition, the absence of ferrite nucleation and growth through the cooling down of S1100 prevented subzones 1 to 5 from any hardness decrease compared to the base material (further discussion is provided in section 4.2).

Furthermore, the combination of bainite and martensite as the microstructures of these zones resulted in a moderate increase in the hardness values. In addition, by decreasing the peak temperature from zone 1 to 5, the ratio of martensite to bainite constituents and prior austenite grain size increased and decreased, respectively (Figs. 6 and 7). These phenomena resulted in a hardness increase in subzone 1 and relatively small hardness fluctuations from zone 1 to 5. Finally, some traces of autotempered martensite was also detected in these regions. However, this constituent did not cause any drastic changes in the mechanical properties of these subzones, as shown in section 4.2.

Regarding subzone 6, the peak temperature is slightly higher than A1, and the material is partially austenitized through its heating stage. Thus, the final microstructure is expected to be a mixture of fresh martensite originated from the partial austenitization and a mixture of tempered martensite and bainitic ferrite due to the tempering of the initial microstructure (Fig. 7 (b, b')). The tempered microstructural features resulted in a sudden drop in the hardness value in subzone 6 compared to its predecessors. However, the hardness decrease is not too severe to cause a softened spot in

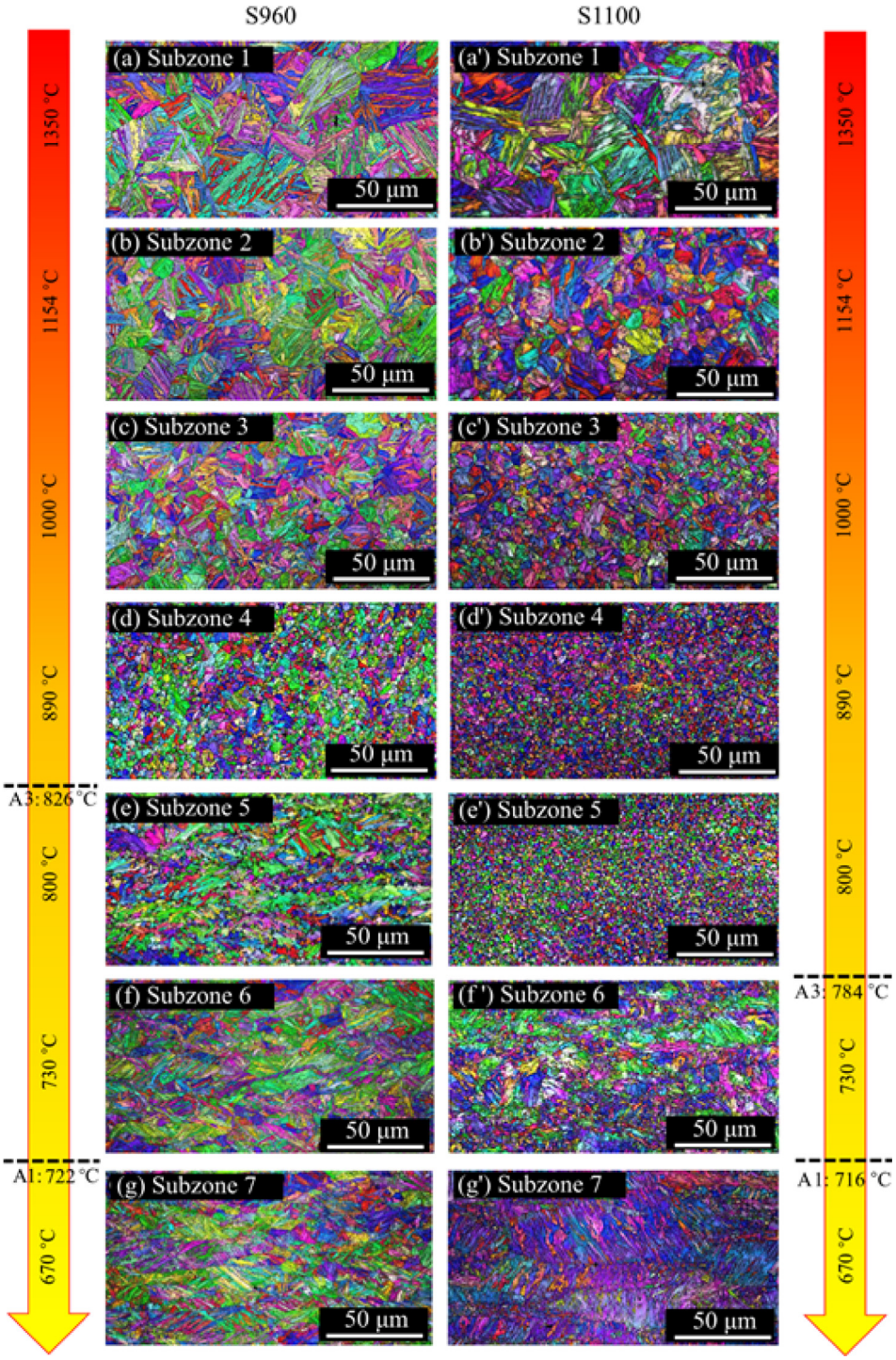

Fig. 8. IPF maps of subzones 1–7 for S960 (a-g) and S1100 (a'-g') along with the pick temperatures indicated on the side arrows.

the HAZ as the hardness value is close to that of the base material (Section 4.2). Finally, heating S1100 up to 670 °C and cooling it down did not cause any significant microstructural changes in this material in subzone 7 (Fig. 7 (c, c')).

4.1. EBSD and quantitative phase analysis

Depending on the distance from the fusion line, each subzone experienced a unique thermal cycle, peak temperature, and $\Delta t_{8/5}$, as described in Table 1. As examples, the cooling paths of subzones 1 and 4 are highlighted by dashed red lines on the CCT diagrams of S960 and S1100 (Figs. 15 and 16, respectively). According to the calculated CCT diagrams, the austenitization-start temperature (A1) for S960 was 722 °C which was slightly higher than that of S1100 (716 °C). However, the difference in austenitization-finish temperatures (A3) was significant as they were estimated at 826 °C for S960 and 783 °C for S1100. Accordingly, as illustrated in Fig. 8 using the IPF maps, in the case of S960, only subzones 1 to 4 experienced full austenitization during their heating. Regarding S1100, in addition to subzones 1 to 4, subzone 5 also reached

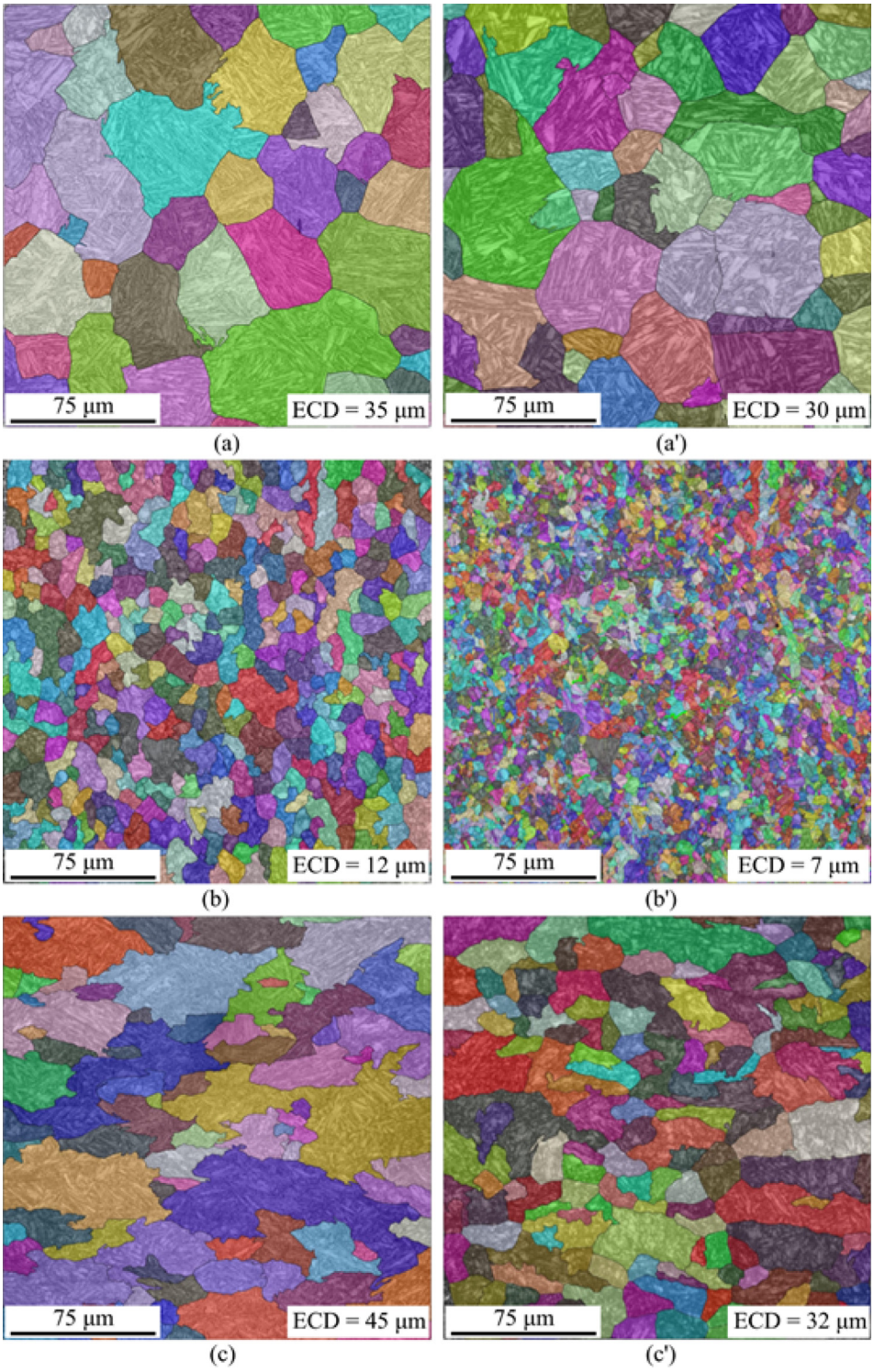

Fig. 9. The reconstructed IPF maps showing prior austenite grain size for the subzones 1, 4, 6: S960 (a-c) and S1100 (a'-c').

the temperature range of full austenitization. The extra fully austenitized subzone in S1100 occurred due to the lower A3 of this steel than S960.

According to EBSD results, the elongated texture of the BM was eliminated in the fully austenitized subzones, and new equiaxed grains were formed throughout these regions in either of the base materials. For a better illustration, the prior austenite structures of subzones 1, 4, and 6 are reconstructed from the IPF maps and presented in Fig. 9. Since grain growth is a temperature–time-dependent phenomenon, prior austenite grain size decreased gradually by decreasing the peak temperature in both alloys. However, due to composition differences, S1100 showed a more refined grain structure in all the conditions. The ECD values from the measurements can be found in Fig. 9. In addition, both 0.2% proof stress and tensile strength of the subzones 1 to 4 progressively increased by the gradual decrease in the prior austenite grain size in both of the materials, as shown in section 4.2.

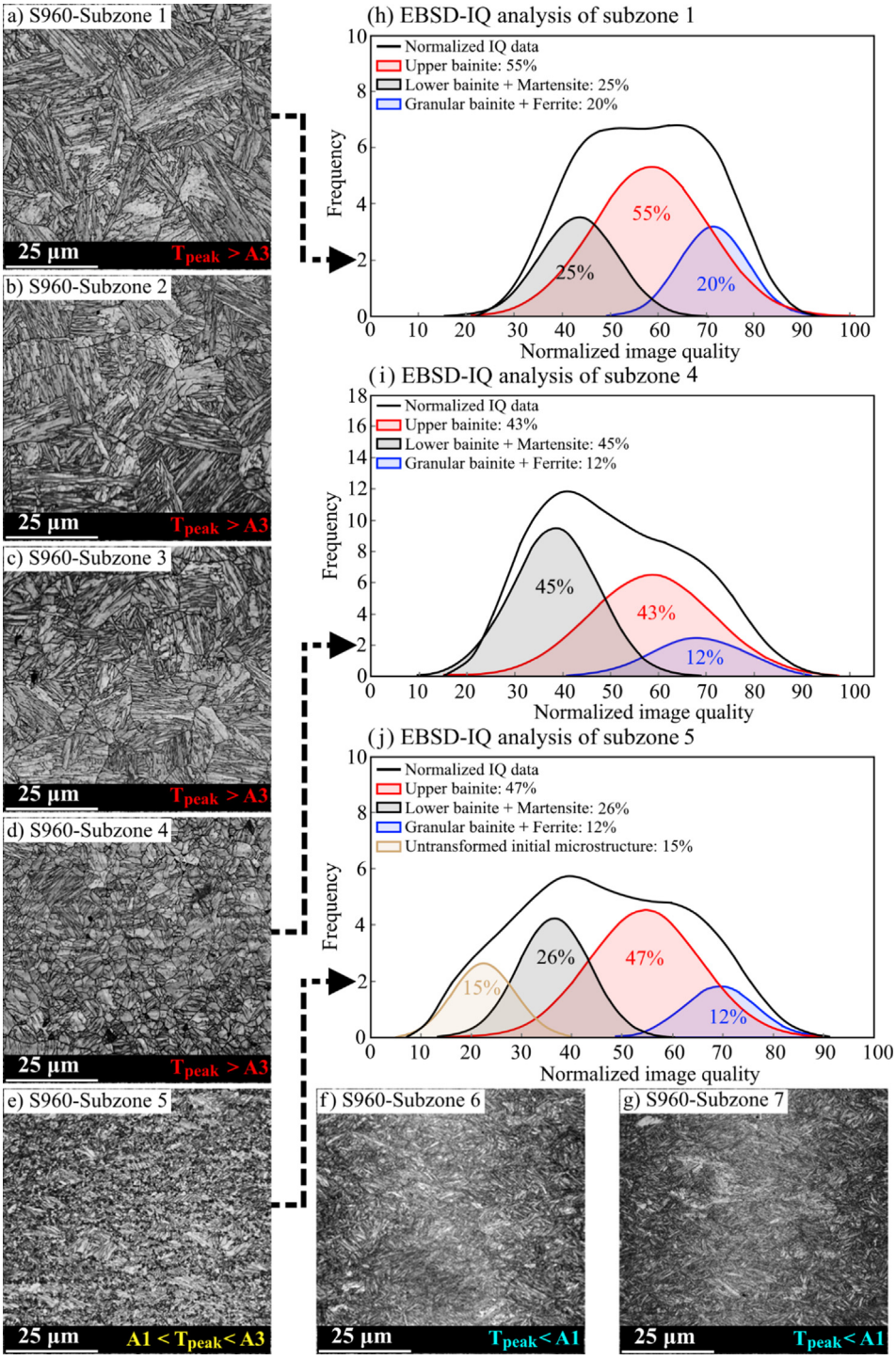

Fig. 10. IQ data of subzones 1–7 (a- g) along with three examples of the normalized IQ values and their phase fraction analysis for (h) subzone 1, (i) subzone 4, and (j) subzone 5.

Regarding the IQ data, the IQ images and their subsequent IQ curves varied by differing the applied thermal cycles on the different subzones, as shown in Section 3.2. The image qualities of the S1100 samples were analyzed in the same way as S960. The results for both alloys are summarized in Fig. 11. In addition to the large fraction of upper and lower types of bainite observed in both alloys, S960 consisted of a considerable amount of high transformation-temperature products of ferrite/granular bainite compared to S1100 (which did not reveal any sign of ferrite formation). Instead, S1100 was comprised of a notable amount of fresh martensite due to its significantly lower martensite-start temperature (Ms) than that of S960 (critical temperature of martensite formation can be found in Figs. 15 and 16).

4.2. Correlations between the microstructural evolutions and mechanical properties

HAZ subzones of both S960 and S1100 consisted of areas with different microstructural features according to their peak temperature and cooling rate during the Gleeble-simulated welding

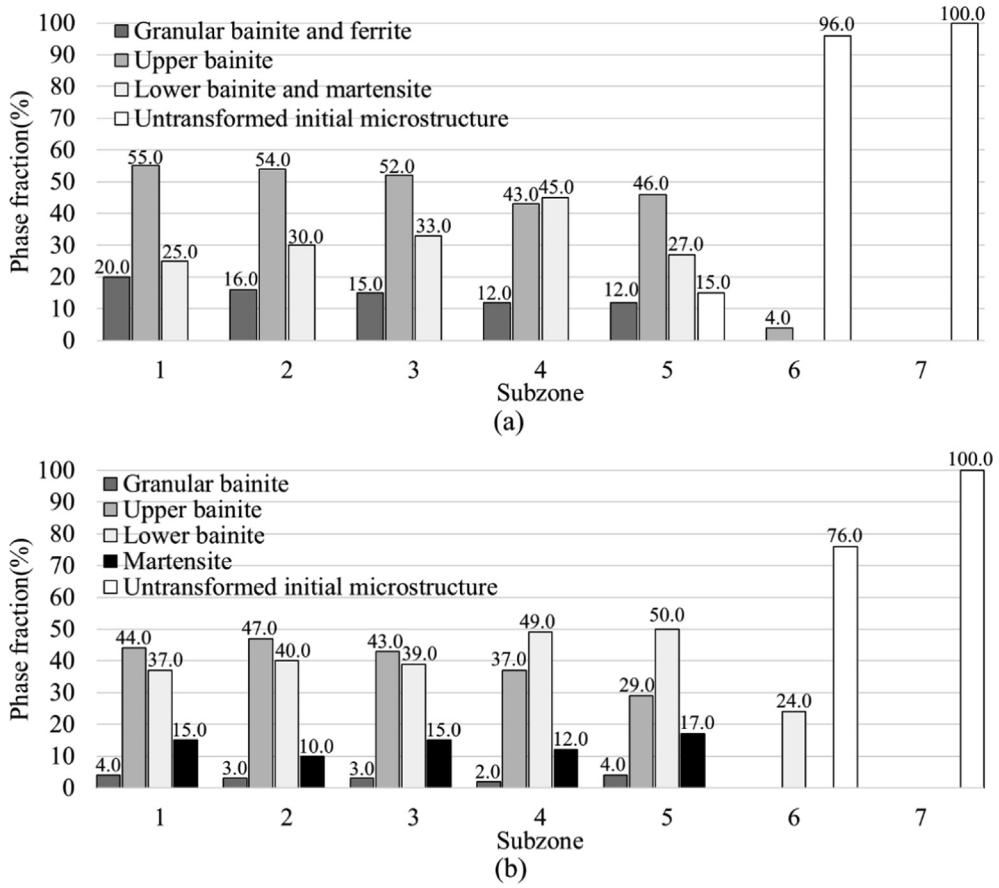

Fig. 11. Phase fraction analysis in detail according to the IQ evaluation for (a) S960 and (b) S1100.

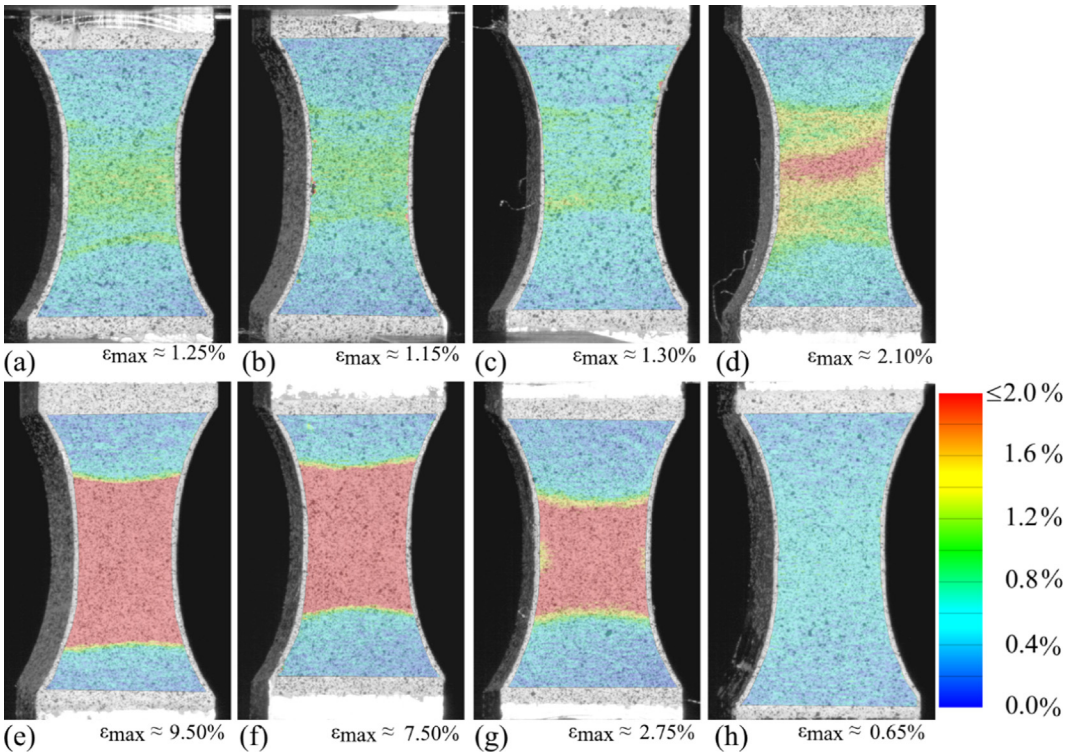

Fig. 12. Local equivalent Mises strains of S960 subzones under the fixed load value of 25.8 kN: (a) subzone 1, (b) subzone 2, (c) subzone 3, (d) subzone 4, (e) subzone 5, (f) subzone 6, (g) subzone 7, and (h) the base metal.

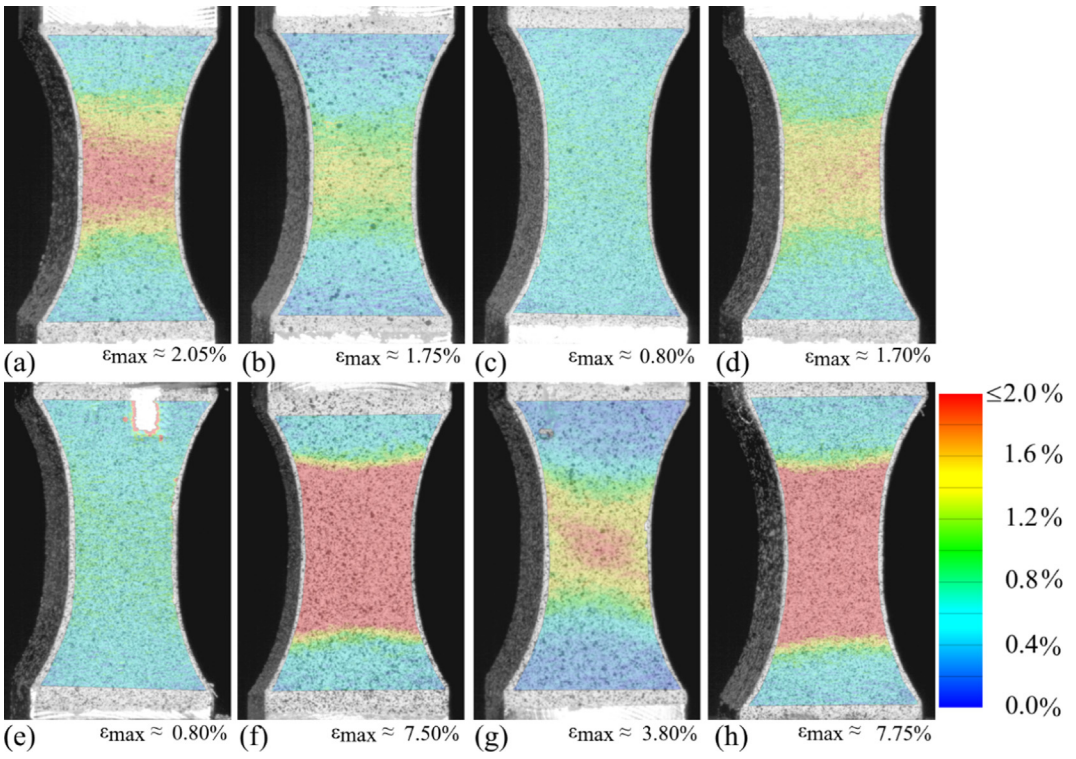

Fig. 13. Local equivalent Mises strains of S1100 subzones under the fixed load value of 36.4 kN: (a) subzone 1, (b) subzone 2, (c) subzone 3, (d) subzone 4, (e) subzone 5, (f) subzone 6, (g) subzone 7, and (h) the base metal.

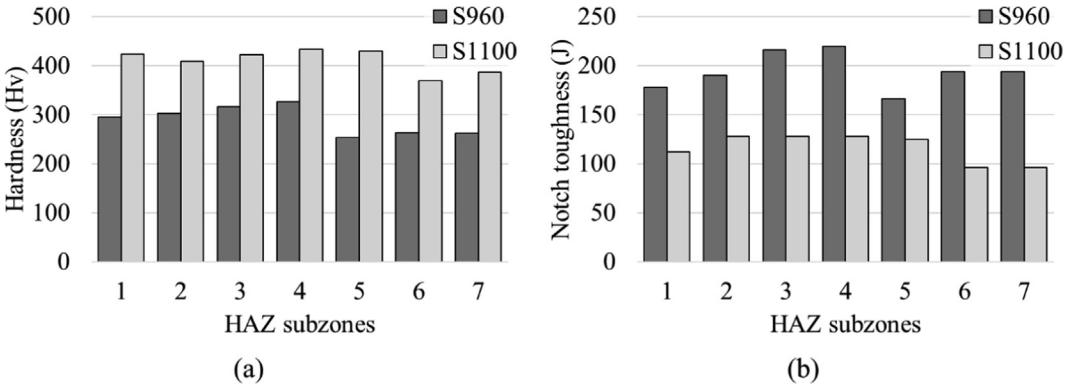

Fig. 14. (a) Hardness and (b) notch toughness values of the simulated HAZ subzones [11].

process. Different microstructures result in different mechanical properties; thus, these subzones are expected to show different behavior under mechanical loads. Fig. 17 for S960 shows that all the HAZ subzones had lower hardness values than the base material (the hardness ratios were smaller than one). However, the drastic hardness decrease occurred in subzone 5, with an approximately 30% drop due to ferrite/granular bainite formation. Next, subzones 6 and 7 had the lowest hardness values due to tempered martensite and bainitic ferrite formation. The quasi-static tensile behavior of the subzones also followed their hardness trend. Subzone 5, which had the lowest hardness, revealed the lowest tensile strength. Hence, the highest local plastic strain under a fixed load is associated with this subzone, as shown in Fig. 12. The fixed load is the load at the tensile strength of the weakest specimen for each steel grade. All the specimens underwent plastic strains at this load, except the base material, and this trend demonstrates softening behavior. This behavior is crucial for designing welded structures since it poses a potential for premature failure at the HAZ.

Contrary to S960, all the subzones of S1100, except number six, had hardness values higher than that of the base material (with hardness ratios greater than one in Fig. 17). Although the hardness drop of subzone 6 was not significant compared to the results of S960, the maximum local plastic strain in this subzone was significantly higher than that of others. According to Fig. 13, the maximum plastic strains and their distribution for both subzone 6 and the base material are relatively similar. This behavior contrasts the assumption on welded UHSS where softened HAZ is considered to govern the failure and dictate the overall performance of the joint. As proved by Amraei et al. [7], considering the von Mises

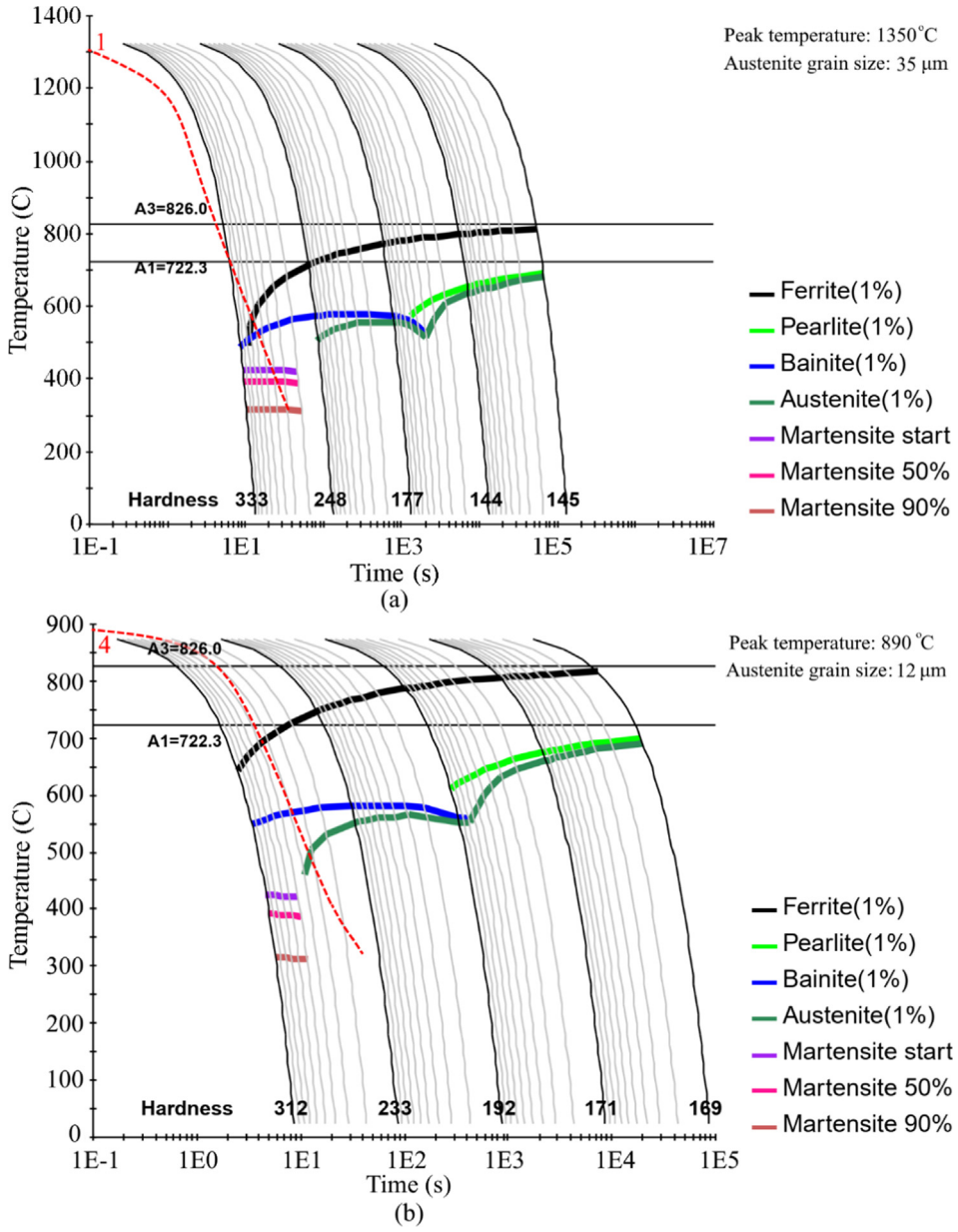

Fig. 15. Theoretical CCT diagrams of S960 for the points with the highest (a) and lowest (b) full austenitization temperatures (subzones 1 and 4, respectively) plotted via JMatPro.

criterion for the failure, the surrounding material of the soft region plays a vital role in creating a boundary condition that can enhance the overall performance of the weldment. The size of the soft region is also of importance preventing the plastic strains from local concentration and piling up. Hence, a firm boundary condition surrounding a narrow softened subzone can result in failure outside the soft area, i.e., the base material. In welded S1100, subzones 1–5 have tensile and hardness values higher than the base material, and only subzone 6 shows a minor softening. Thus, the final failure in welded S1100 typically occurs at the base material [2].

The hardness value of carbon steel can be estimated after its continuous cooling based on the chemistry, microstructure, and thermal condition of the material; and, there are various models available for this purpose [31–33]. In this section, two models, a regression type and a best-fit one, are tested against the experimental data. The regression model developed by Maynier et al. [32] can be expressed as follows:

$$HV_m = 127 + 949C_{wt\%} + 27Si_{wt\%} + 11Mn_{wt\%} + 16Cr_{wt\%} + 8Ni_{wt\%} + 21\log_{10}V_R \quad (1)$$

$$HV_b = -323 + 185C_{wt\%} + 330Si_{wt\%} + 153Mn_{wt\%} + 144Cr_{wt\%} + 191Mo_{wt\%} + 65N_{wt\%} + \log_{10}V_R(89 + 53C_{wt\%} - 55Si_{wt\%} - 22Mn_{wt\%} - 20Cr_{wt\%} - 33Mo_{wt\%} - 10Ni_{wt\%}) \quad (2)$$

$$HV_f = 42 + 223C_{wt\%} + 53Si_{wt\%} + 30Mn_{wt\%} + 7Cr_{wt\%} + 19Mo_{wt\%} + 12.6Ni_{wt\%} + \log_{10}V_R(10 - - 19Si_{wt\%} + 8Cr_{wt\%} + 4Ni_{wt\%} + 130V_{wt\%}) \quad (3)$$

where HV_m, HV_b, and HV_f are the Vickers hardness values of martensite, bainite, and ferrite, respectively, and V_R is the cooling rate after austenitization (°C/h). The following linear rule of mixtures gives the final hardness of steel:

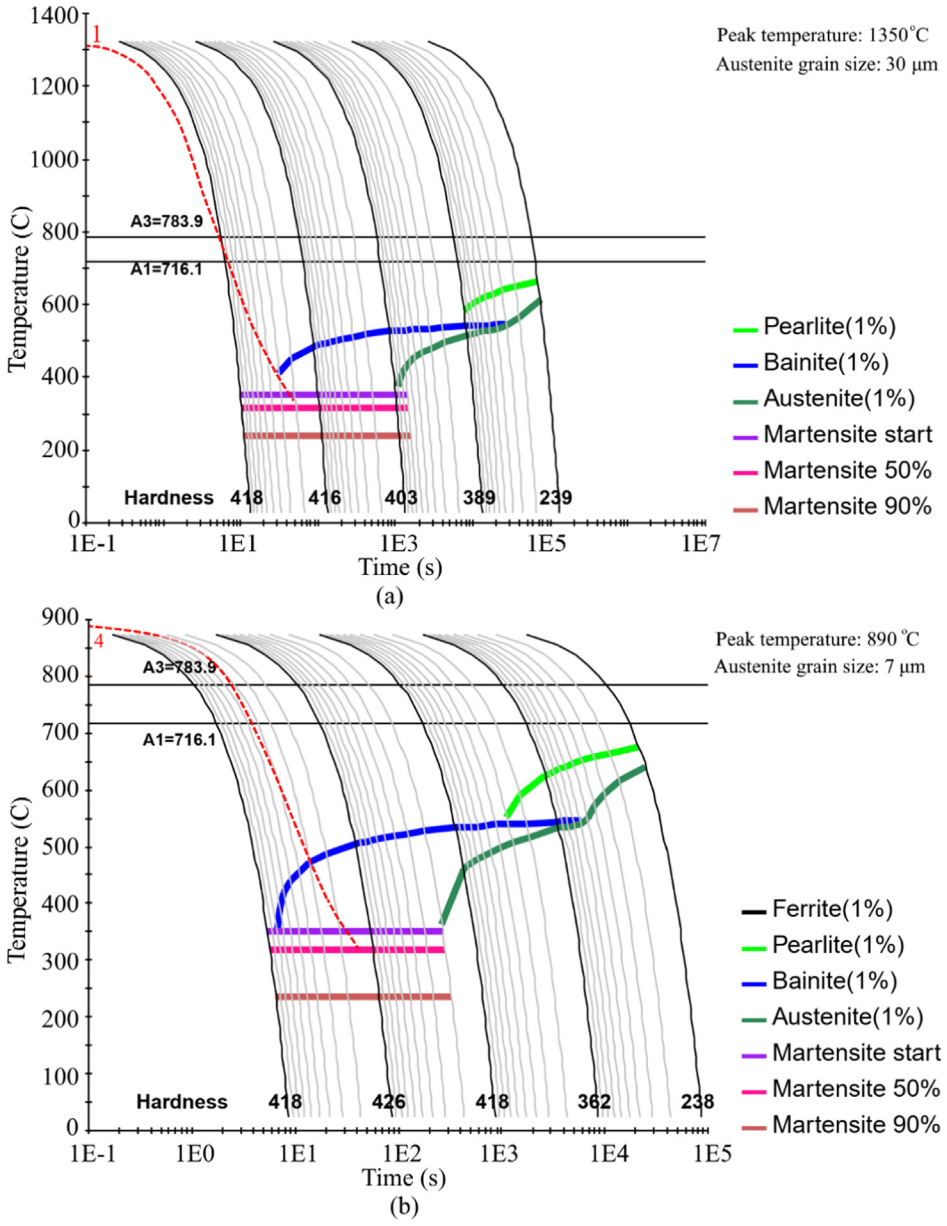

Fig. 16. Theoretical CCT diagrams of S1100 for subzones 1 (a) and 4 (b) plotted via JMatPro.

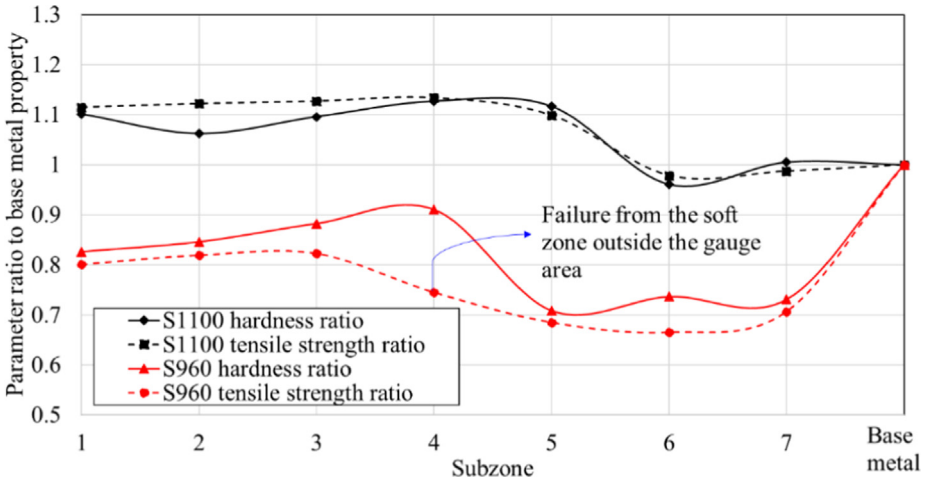

Fig. 17. Hardness fluctuations for different HAZ subzones [11].

$$HV = f_f(HV_f) + f_b(HV_b) + f_m(HV_m) \quad (4)$$

where f_f, f_b, and f_m are the fractions of ferrite, bainite, and martensite, respectively. In this study, fractions of granular bainite were also accounted for in f_f calculations due to the similar properties and characteristics of granular bainite and ferrite. The presence of lower bainite and martensite were also accounted for together in f_m calculations due to the same reason.

The best-fit model, developed by Pohjonen et al. [33] for bearing steel with 0.2 $C_{wt\%}$, is as follows:

$$HV = f_b(C + A\log_{10}V_R) + f_m HV_m \quad (5)$$

where C and HV_m are the fitting parameters, and A is a material dependant constant that can be calculated via Eq. (6):

$$A = 89 + 53C_{wt\%} - 55Si_{wt\%} - 22Mn_{wt\%} - 10Ni_{wt\%} - 20Cr_{wt\%} - 33Mo_{wt\%}$$

Similar to the regression model, granular bainite and lower bainite contributions in the hardness values were accounted for in the f_b and f_m fractions, respectively. The fitted C and HV_m values were 30 and 370 for S960, and 400 and 400 for S1100, respectively. The effects of austenite grain size and homogeneity are neglected in both models since they do not consider austenitizing temperature and heating time in their calculations.

Fig. 18 shows comparisons of the experimental results presented in Section 3.3 with the predictions made by the models. According to the results and comparisons, different thermal cycles of the different subzones lead to different microstructures and, consequently, different hardness levels. Pohjonen's model showed slightly better results than the other model; however, both models deviated from the experimental measurements regarding the subzones with T_{peak} between A1 and A3 or lower than A1. Despite the deviations, both models seem to be equally acceptable for the practical use to detect the softened HAZ of either welded structural steels and UHSS.

Regarding the notch toughness values, the results seemed controversial at first sight. Typically, Charpy notch toughness and hardness have a reverse correlation with each other. However, in this study, subzones with the minimum hardness also had the lowest notch toughness values, as shown in Fig. 14. This behavior can be attributed to the existence of tempered martensite and bainitic ferrite in the softened areas. Although these microstructural features have relatively low hardness values due to the existence of ferrite, carbides in the tempered martensite precipitated along the bainitic ferrite boundaries and encouraged more brittle fractures in the Charpy test. Thus, areas such as subzone 5 in S960 and 6 in S1100 suffered from the simultaneous decrease of hardness and notch toughness values.

5. Conclusions

Thermo-mechanical simulations using Gleeble 3800 were performed to replicate seven HAZ subzones of S960 and S1100 structural steels. Then, the microstructural transformations, their mechanisms, and the resultant microstructures were studied. The correlations between the microstructure and mechanical properties were also comprehensively studied, as schematically shown in Fig. 19, based on the peak temperatures and cooling rates experienced during the welding process. According to the results, the following conclusions are drawn:

- Depending on the distance from the fusion line and its subsequent peak temperature, HAZ subzones of UHSS with properties different from their base metals can fit into three groups: fully austenitized (T_{peak} > A3), partially austenitized (A1 < T_{peak} < A3), and tempered (T_{peak} < A1).
- In the fully austenitized subzones, the prior austenite grain size decreased by increasing the distance from the fusion line.
- Decrease in the contents of lower bainite and martensite, as hard microstructural mixtures, and their replacement by softer mixtures of upper bainite, granular bainite, and ferrite resulted in soft spots in the HAZ, typically known as softened HAZ.

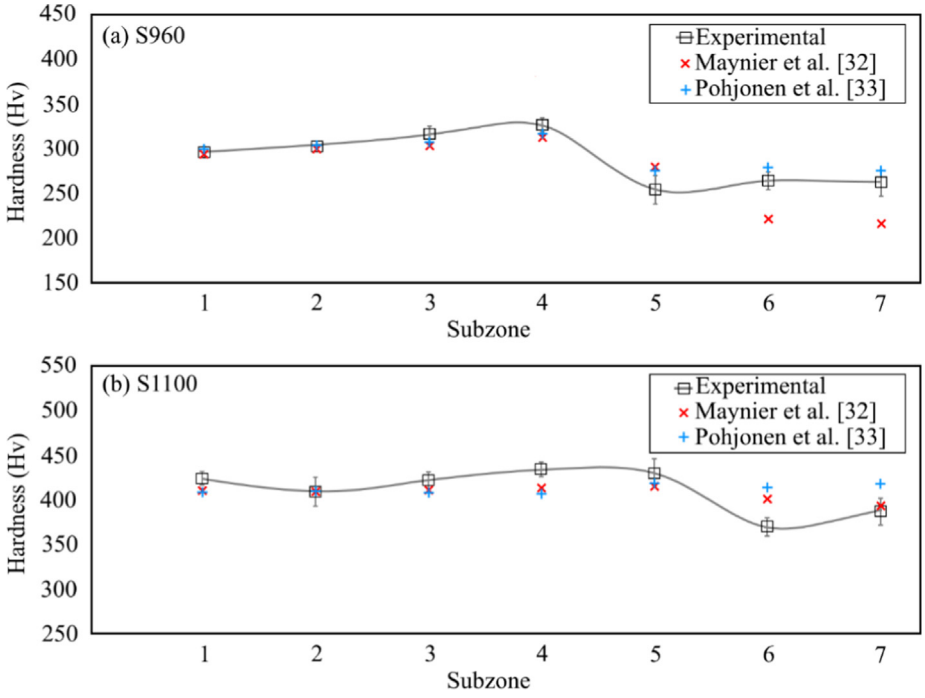

Fig. 18. The calculated hardness values for the different subzones along with the average value from the experimental measurements.

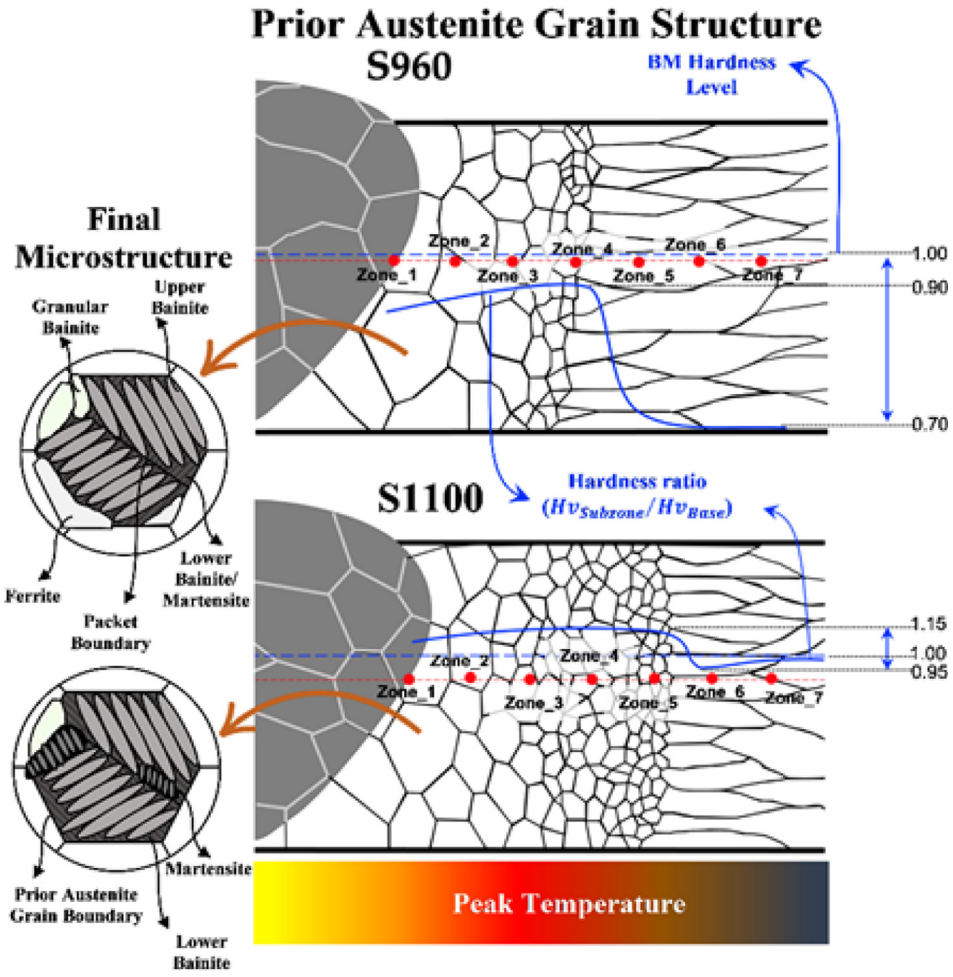

Fig. 19. Schematic illustration of the prior austenite grain structure changes at the different subzones for both alloys and the resulted hardness value based on the final microstructure (an example of the final microstructures is illustrated for subzone 1).

- According to the CCT diagrams, hindering and avoiding ferrite formation in UHSS can preserve the mechanical properties after welding, e.g., the case of S1100.
- Analyzing EBSD-IQ data from UHSS with complex microstructures proved to be a relatively reliable approach to quantitatively identifying their microstructures.
- There was a good agreement between the hardness values and local strains of the subzones. Regarding the notch toughness, this property reached its minimum level in the softest subzones. The controversial simultaneous decrease of hardness and toughness in such areas was attributed to the tempered martensite and bainite in these regions.
- Hardness models proposed by Maynier et al. [1] and Phjonen et al. [2] effectively predicted the locations of the softened spots in the HAZs of UHSS. However, there were slight fluctuations between the actual and predicted values at the regions where peak temperatures were below A3.

In conclusion, although hardness decrease seems to be a drawback for certain welded UHSS grades, it can be hindered by delaying ferrite formation in these steels. Modifications in chemical composition and initial microstructure by adjusting the manufacturing process of steel might assist in achieving such a purpose, similar to S1100. In addition, it is possible to minimize the adverse effect of the softened zone on the overall performance of welded joints by reducing the size of the subzone and restricting it between its adjacent regions with better mechanical properties (improving the boundary condition). Finally, the simultaneous decrease in toughness and hardness in the softened HAZ might raise another concern regarding welded UHSS, which requires further research, especially in cryogenic applications. Regarding this matter, thorough investigations similar to the current study but in cryogenic conditions seem vital to approve the reliability of welded UHSS on a broader domain of industrial applications.

Data Availability Statement

The raw/processed data required to reproduce these findings can be obtained upon request from the corresponding author.

Declaration of Competing Interest

The authors declare that they have no known competing financial interests or personal relationships that could have appeared to influence the work reported in this paper.

Acknowledgment

The authors wish to thank SSAB Europe Co. for providing the base materials used in this research. The help and support of Mr. Matti Koskimäki and Prof. Jari Larkiola for managing the experimental procedures, Mr. Juha Uusitalo in performing the Gleeble simulations, and Mr. Toni Väkiparta in conducting the SEM are highly appreciated. The authors also extend special thanks for the technical support provided by the staff members at the laboratories of LUT Steel Structures and Welding Technology.

Vahid Javaheri would also like to thank Jenny and Antti Wihuri Foundation for the personal financial support.

References

[1] B.A. Burgan, M.R. Sansom, Sustainable steel construction, J. Constr. Steel Res. 62 (11) (2006) 1178–1183, https://doi.org/10.1016/j.jcsr.2006.06.029.

[2] M. Amraei, A. Ahola, S. Afkhami, T. Björk, A. Heidarpour, X.L. Zhao, Effects of heat input on the mechanical properties of butt-welded high and ultra-high strength steels, Eng. Struct. 198 (2019), https://doi.org/10.1016/j.engstruct.2019.109460 109460.

[3] S. Afkhami, T. Björk, J. Larkiola, Weldability of cold-formed high strength and ultra-high strength steels, J. Constr. Steel Res. 158 (2019) 86–98, https://doi.org/10.1016/j.jcsr.2019.03.017.

[4] S. Mandal, N.K. Tewary, S.K. Ghosh, D. Chakrabarti, S. Chatterjee, Thermo-mechanically controlled processed ultrahigh strength steel: Microstructure, texture and mechanical properties, Mater. Sci. Eng. A. 663 (2016) 126–140, https://doi.org/10.1016/j.msea.2016.03.127.

[5] S. K., R. Kawall, Ultrahigh Strength Steel: Development of Mechanical Properties Through Controlled Cooling, in: Heat Transf. - Eng. Appl., InTech, 2011. 10.5772/26514.

[6] S. Keeler, M. Kimchi, P.J. Mooney, Advanced High-Strength Steels Application Guidelines Version 6 (2017). https://www.worldautosteel.org/projects/advanced-high-strength-steel-application-guidelines/.

[7] M. Amraei, M. Dabiri, T. Björk, T. Skriko, Effects of Workshop Fabrication Processes on the Deformation Capacity of S960 Ultra-high Strength Steel, J. Manuf. Sci. Eng. Trans. ASME. 138 (2016), https://doi.org/10.1115/1.4033930.

[8] F. Farrokhi, J. Siltanen, A. Salminen, Fiber Laser Welding of Direct-Quenched Ultrahigh Strength Steels: Evaluation of Hardness, Tensile Strength, and Toughness Properties at Subzero Temperatures, J. Manuf. Sci. Eng. Trans. ASME. 137 (2015), https://doi.org/10.1115/1.4030177.

[9] W. Guo, D. Crowther, J.A. Francis, A. Thompson, Z. Liu, L. Li, Microstructure and mechanical properties of laser welded S960 high strength steel, Mater. Des. 85 (2015) 534–548, https://doi.org/10.1016/j.matdes.2015.07.037.

[10] W. Guo, L. Li, D. Crowther, S. Dong, J.A. Francis, A. Thompson, Laser welding of high strength steels (S960 and S700) with medium thickness, J. Laser Appl. 28 (2016), https://doi.org/10.2351/1.4944100 022425.

[11] M. Amraei, S. Afkhami, V. Javaheri, J. Larkiola, T. Skriko, T. Björk, X.L. Zhao, Mechanical properties and microstructural evaluation of the heat-affected zone in ultra-high strength steels, Thin-Walled Struct. 157 (2020), https://doi.org/10.1016/j.tws.2020.107072 107072.

[12] J. Brabec, Š. Ježek, L. Beneš, A. Kříž, P. Majrich, Suitability Confirmation for Welding Ultra-High Strength Steel S1100QL Using the RapidWeld Method, Manuf. Technol. 21 (2021) 29–36. 10.21062/mft.2021.014.

[13] A. Su, Y. Liang, O. Zhao, Experimental and numerical studies of S960 ultra-high strength steel welded I-section columns, Thin-Walled Struct. 159 (2021), https://doi.org/10.1016/j.tws.2020.107166 107166.

[14] A.K. Pramanick, H. Das, J.W. Lee, Y. Jung, H.H. Cho, S.T. Hong, M. Shome, A.K. Pramanick, Texture analysis and joint performance of laser-welded similar and dissimilar dual-phase and complex-phase ultra-high-strength steels, Mater. Charact. 174 (2021), https://doi.org/10.1016/j.matchar.2021.111035 111035.

[15] T. Skriko, K. Lipiäinen, A. Ahola, H. Mettänen, T. Björk, Fatigue strength of longitudinal load-carrying welds in beams made of ultra-high-strength steel, J. Constr. Steel Res. 179 (2021), https://doi.org/10.1016/j.jcsr.2021.106563 106563.

[16] H. Jiao, X.L. Zhao, A. Lau, Hardness and compressive capacity of longitudinally welded very high strength steel tubes, J. Constr. Steel Res. 114 (2015) 405–416, https://doi.org/10.1016/j.jcsr.2015.09.008.

[17] K. Wallin, S. Pallaspuro, I. Valkonen, P. Karjalainen-Roikonen, P. Suikkanen, Fracture properties of high performance steels and their welds, Eng. Fract. Mech. 135 (2015) 219–231, https://doi.org/10.1016/j.engfracmech.2015.01.007.

[18] S. Pallaspuro, H. Yu, A. Kisko, D. Porter, Z. Zhang, Fracture toughness of hydrogen charged as-quenched ultra-high-strength steels at low temperatures, Mater. Sci. Eng. A. 688 (2017) 190–201, https://doi.org/10.1016/j.msea.2017.02.007.

[19] L. Tong, L. Niu, S. Jing, L. Ai, X.L. Zhao, Low temperature impact toughness of high strength structural steel, Thin-Walled Struct. 132 (2018) 410–420, https://doi.org/10.1016/j.tws.2018.09.009.

[20] H. Bhadeshia, R. Honeycombe, Heat Treatment of Steels: Hardenability, in: Steels Microstruct. Prop., Elsevier, 2017: pp. 217–236. 10.1016/b978-0-08-100270-4.00008-1.

[21] V. Javaheri, A. Pohjonen, J.I. Asperheim, D. Ivanov, D. Porter, Physically based modeling, characterization and design of an induction hardening process for a new slurry pipeline steel, Mater. Des. 182 (2019), https://doi.org/10.1016/j.matdes.2019.108047 108047.

[22] V. Javaheri, S. Pallaspuro, A. Kaijalainen, S. Sadeghpour, J. Kömi, D. Porter, Promising bending properties of a new as-rolled medium-carbon steel achieved with furnace-cooled bainitic microstructures, Mater. Sci. Eng. A. 796 (2020), https://doi.org/10.1016/j.msea.2020.140011.

[23] H. Tervo, A. Kaijalainen, V. Javaheri, S. Kolli, T. Alatarvas, S. Anttila, J. Kömi, Characterization of coarse-grained heat-affected zones in al and ti-deoxidized offshore steels, Metals (Basel). 10 (2020) 1–18, https://doi.org/10.3390/met10081096.

[24] A.J. DeArdo, C.I. Garcia, K. Cho, M. Hua, New method of characterizing and quantifying complex microstructures in steels, Mater. Manuf. Process. 25 (1-3) (2010) 33–40, https://doi.org/10.1080/10426910903143415.

[25] J. Wu, P.J. Wray, C.I. Garcia, M. Hua, A.J. Deardo, Image quality analysis: A new method of characterizing microstructures, ISIJ Int. 45 (2005) 254–262, https://doi.org/10.2355/isijinternational.45.254.

[26] ASTM Int. (2018) 1–26, https://doi.org/10.1520/E0023-18.

[27] A. Navarro-López, J. Hidalgo, J. Sietsma, M.J. Santofimia, Characterization of bainitic/martensitic structures formed in isothermal treatments below the Ms temperature, Mater. Charact. 128 (2017) 248–256, https://doi.org/10.1016/j.matchar.2017.04.007.

[28] S.I. Wright, M.M. Nowell, EBSD Image Quality Mapping, Microsc. Microanal. 12 (01) (2006) 72–84, https://doi.org/10.1017/S1431927606060090.

[29] X. Tao, A. Eades, Alternatives to Image Quality (IQ) Mapping in EBSD, Microsc. Microanal. 8 (S02) (2002) 692–693, https://doi.org/10.1017/S1431927602106465.

[30] A.J. DeArdo, M.J. Hua, K.G. Cho, C.I. Garcia, On strength of microalloyed steels: an interpretive review, Mater. Sci. Technol. 25 (9) (2009) 1074–1082, https://doi.org/10.1179/174328409X455233.

[31] J. Trzaska, Calculation of the steel hardness after continuous cooling, Arch. Mater. Sci. Eng. 61 (2013) 87–92.

[32] P. Maynier, B. Jungmann, J. Dollet, Creusot-Loire system for the prediction of the mechanical properties of low alloy steel products, in, Hardenability Concepts with Appl. to Steel (1997) 518–545.

[33] A. Pohjonen, M. Somani, D. Porter, Modelling of austenite transformation along arbitrary cooling paths, Comput. Mater. Sci. 150 (2018) 244–251, https://doi.org/10.1016/j.commatsci.2018.03.052.